

# Plant Polyphenol-Assisted Green Synthesis of Hollow CoPt Alloy Nanoparticles for Dual-Modality Imaging Guided Photothermal Therapy

Xiao-Rong Song, Shu-Xian Yu, Gui-Xiao Jin, Xiaoyong Wang, Jianzhong Chen, Juan Li, Gang Liu,\* and Huang-Hao Yang\*

*Theranostic nanomedicines that integrate diagnostic and therapeutic moieties into a single nanoscale platform are playing an increasingly important role in fighting cancer. Here, a facile and green synthetic strategy for hollow CoPt alloy nanoparticles (HCPA-NPs) using plant polyphenols as assisted agents is reported for the first time. This novel strategy enables size-controlled synthesis of HCPA-NPs through the control of the molecular sizes of polyphenols. It is also a versatile strategy for synthesizing other hollow alloy nanoparticles with various metal compositions due to the diverse metal-chelating ability of the polyphenols. Further studies show that HCPA-NPs have good biocompatibility and can be successfully implemented for magnetic resonance and photoacoustic dual-modal imaging guided photothermal therapy. This work brings new insights for the green synthesis of hollow nanoparticles and extends these biocompatible nanoparticles for theranostic applications.*

## 1. Introduction

The combination of nanotechnology and cancer theranostic has achieved great developments in the past few years.<sup>[1]</sup> Nanomaterials have many merits in biomedical applications, such as prolonged circulation time and easy functionalization.

X.-R. Song, S.-X. Yu, G.-X. Jin, Prof. J. Z. Chen,  
Dr. J. Li, Prof. H.-H. Yang  
The Key Lab of Analysis and Detection Technology  
for Food Safety of the MOE  
State Key Laboratory of Photocatalysis on Energy  
and Environment  
College of Chemistry  
Fuzhou University  
Fuzhou 350108, China  
E-mail: hhyang@fio.org.cn

Dr. X. Y. Wang, Prof. G. Liu  
State Key Laboratory of Molecular Vaccinology and Molecular  
Diagnostics  
Center for Molecular Imaging and Translational Medicine  
School of Public Health  
Xiamen University  
Xiamen 361005, China  
E-mail: gangliu.cmitm@xmu.edu.cn  
DOI: 10.1002/sml.201503250



Furthermore, theranostic nanomaterials enable improved treatment efficacy of cancer by multimodal image-guided combination therapy.<sup>[2]</sup> **Hollow nanoparticles are an important type of theranostic nanomaterials due to their low density, reduced material use, and low costs.**<sup>[3]</sup> Moreover, the large pore volumes as well as the distinct properties of magnetism, electronics, and optics make hollow nanoparticles useful as a multifunctional platform for theranostic nanomedicines.<sup>[4]</sup>

Despite substantial advances in the synthesis of nanomaterials, there are still some drawbacks that must be addressed. **For example, the use of toxic or expensive reagents as stabilizing agents and structure-directing agents for nanomaterials synthesis may cause health and environmental issues.**<sup>[5]</sup> Furthermore, the common synthetic strategy for hollow nanomaterials must use hard template materials, and one necessary step is the removal of the template.<sup>[6]</sup> This post-treatment not only increases complexity and cost to the system, but also deforms the hollow structure. Therefore, it is still highly desirable to develop a straightforward and green synthetic strategy for nanomaterials.

Plant polyphenols are compounds with dihydroxyphenyl (catechol) and trihydroxyphenyl (pyrogallol) groups within the molecules. They are beneficial to human health.<sup>[7]</sup> Recently, polyphenols have been utilized as stabilizing ligands or coordinating ligands for the synthesis of solid metal

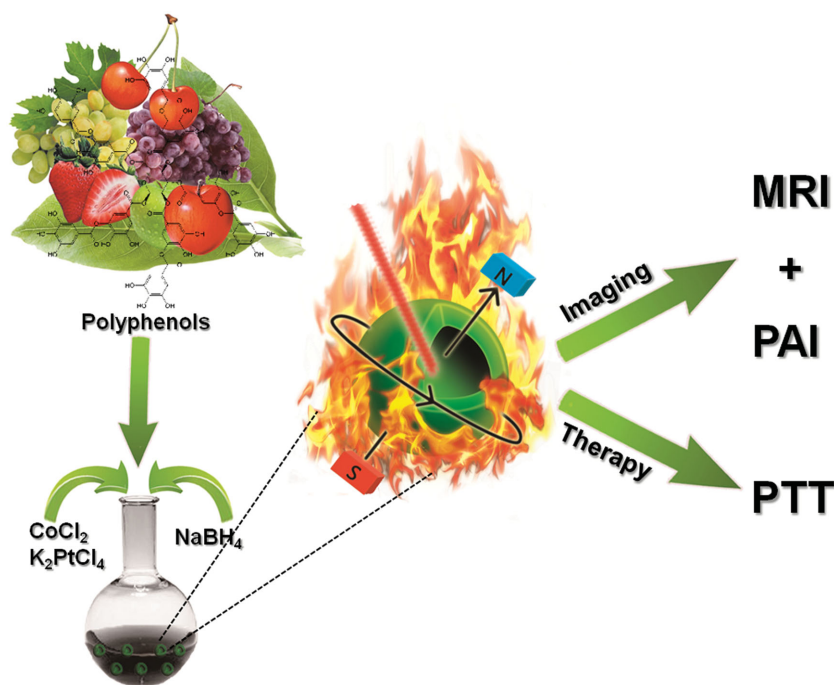


Figure 1. Schematic illustration of the synthesis and theranostic applications of HCPA-NPs.

nanoparticles and metal-phenolic networks.<sup>[8]</sup> However, there has been no report using polyphenols for the preparation of hollow alloy nanoparticles. Recently, some methods have been developed for preparing alloy nanoparticles with various compositions.<sup>[9]</sup> Of note, greener methods with the use of less toxic and more biocompatible agents are desired to obtain alloy nanoparticles with well-defined size and structure, which would be more favorable to biomedical applications. Here we report a facile, green, and size-controlled synthesis of hollow alloy nanoparticles using plant polyphenols as assisted agents (Figure 1). Hollow CoPt alloy nanoparticles (HCPA-NPs) with different sizes were obtained by changing the used polyphenols with different molecule size. The developed method also gives a universal approach to synthesize other alloy nanostructures, such as hollow NiPt alloy. Moreover, the as-prepared HCPA-NPs showed good biocompatibility and high  $T_2$  relaxivity, exhibiting splendid magnetic resonance imaging (MRI) contrast enhancement. Besides, the HCPA-NPs possessed the properties of distinct near-infrared (NIR) absorbance and high photothermal conversion efficiency, which made HCPA-NPs able to be used as a photoacoustic imaging (PAI) contrast agent and a photothermal agent. We successfully employed HCPA-NPs for MRI/PAI dual-modality imaging guided photothermal therapy (PTT) *in vivo*.

## 2. Results and Discussion

HCPA-NPs were synthesized through co-reduction of the aqueous solutions of cobalt (II) chloride and potassium tetrachloroplatinate (II) in the presence of polyphenols by using  $\text{NaBH}_4$  as a reduction agent (Figure 1). We first investigated the effect of metal salt precursors on HCPA-NPs by using tannic acid (TA), a common polyphenol, as an assisted

agent. The transmission electron microscopy (TEM) results from samples with different molar ratios of Co to Pt indicate that hollow structures continue to form with the increase of the molar ratios (Figure S1, Supporting Information). The hollow structure was completely formed when the ratio reached to 1:1. As shown in high-magnification TEM (Figure 2a), the center sections of the nanostructures are brighter than the edge sections, which indicates the formation of hollow structures. The average diameter of the HCPA-NPs is about 20 nm with a shell thickness of about 3 nm. The elemental mapping images in Figure 2b reveal that both Co and Pt are homogeneously distributed in sheath, confirming the hollow morphology of the nanoparticles as well. Energy-dispersive X-ray spectroscopy (EDS) was also used to confirm the chemical composition of the HCPA-NPs (Figure 2c), showing peaks of the elements Pt and Co.

The size-controlled synthesis of HCPA-NPs was also studied by using different

polyphenols as assisted agents. Interestingly, HCPA-NPs with size of  $9.6 \pm 1.2$  nm were obtained when using epigallocatechin gallate (EGCG), which has smaller molecule size and lower amounts of catechol and pyrogallol moieties than TA (Figure 2d). Moreover, a further reduction in particle size of  $6.6 \pm 0.8$  nm was achieved with ellagic acid (EA) as an assisting agent, which has smaller molecule size compared to EGCG (Figure S2, Supporting Information). The particle size distributions of these samples from TEM analysis were shown in Figure S3 (Supporting Information). Furthermore, the versatility of the synthetic strategy was studied by synthesizing hollow NiPt and CoMo alloy nanoparticles under a similar procedure. Figure 2e and Figure S4 (Supporting Information) show the TEM image of the generated hollow NiPt and CoMo alloy nanoparticles with sizes of  $17.6 \pm 2.3$  nm and  $16.7 \pm 1.9$  nm, respectively. The above results demonstrated that the synthetic strategy for hollow alloy nanostructures by using polyphenols as assisted agents has size controllability and versatility.

Although hollow CoPt nanoparticles have been reported in previous articles, our strategy utilized easily available and better biocompatible polyphenols as assisted agents.<sup>[10]</sup> Moreover, the diversity of polyphenolic compounds together with their unique ability to chelate various metals makes the strategy especially appropriate for the synthesis of hollow nanomaterials with different sizes and various compositions. To understand the formation mechanism, we changed the synthetic procedure by firstly adding  $\text{NaBH}_4$  to the mixture of TA and Co salts, immediately followed by the addition of Pt salts. As shown in the TEM image (Figure S5, Supporting Information), only nanostructures with assembled small nanoparticles can be obtained, indicating that the formation mechanism is different from galvanic displacement.<sup>[10c]</sup> Based on the results, we speculate that the formation mechanism of

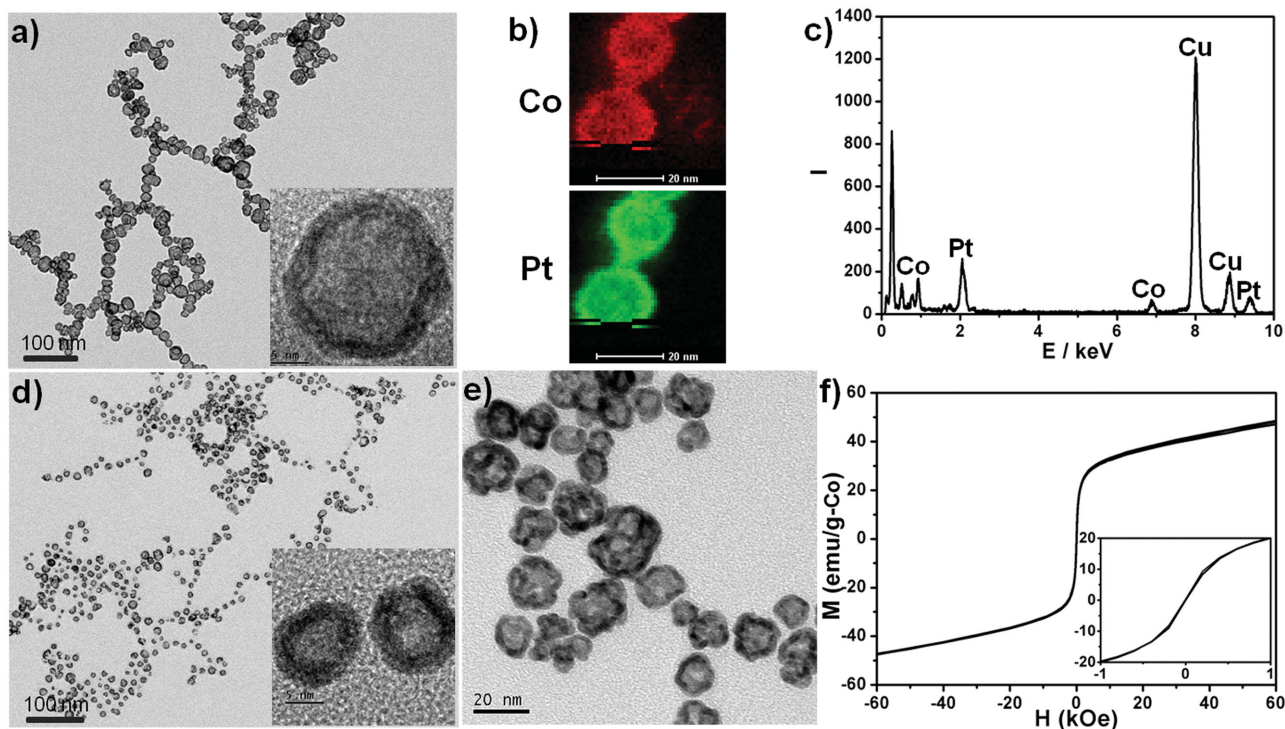


**Figure 2.** a) TEM image of the obtained HCPA-NPs using TA as an assisted agent. Inset: Magnified TEM image of as-prepared HCPA-NPs. b) Elemental mapping images of HCPA-NPs: Co (top) and Pt (bottom) scale bar: 20 nm. c) EDS spectrum of HCPA-NPs. d) TEM image of the obtained HCPA-NPs using EGCG as an assisted agent. Inset: Magnified TEM image of as-prepared HCPA-NPs. e) TEM image of the obtained hollow NiPt nanoparticles using TA as an assisted agent. f) The field-dependent magnetization curve of HCPA-NPs prepared by using TA as assisted agents. Inset: the amplified M–H curve.

hollow nanostructure is polyphenols-directed manner rather than galvanic displacement. A deeper and more careful understanding of the mechanisms will be carried out in our further studies.

To extend the HCPA-NPs to biomedical applications, we functionalized the HCPA-NPs of about 20 nm with polyethylene glycol (HCPA-NPs-PEG), which is a surface ligand typically used for improving the physiological stability of the nanomaterials.<sup>[11]</sup> The HCPA-NPs-PEG has better water solubility than HCPA-NPs (Figure S6, Supporting Information). The dark cytotoxicity of HCPA-NPs-PEG was then studied on HepG2, MCF-7, and HeLa cells by a CCK-8 assay. The results showed that the viabilities of all three types of cells were not significantly affected even when the concentration of HCPA-NPs-PEG reached  $200 \mu\text{g mL}^{-1}$  (Figure 3). These results indicate that the HCPA-NPs-PEG has better biocompatibility and lower toxicity than previously reported cobalt-based nanoparticles, such as Co nanoparticles, Co@Au nanospheres, and CoPt nanoparticles.<sup>[12]</sup> This is possibly due to the good biocompatibility and anti-oxidation potential of polyphenols, which prevent the HCPA-NPs from releasing the toxic cobalt ions.

Although the most commonly used  $T_2$ -weighted MRI contrast agents are superparamagnetic iron oxide nanoparticles (SPIO-NPs), Co nanoparticles are also

effective MRI contrast agents and have their own advantages, such as higher saturation magnetization value than that of SPIO-NPs.<sup>[13]</sup> However, the instability of Co nanoparticles in the biological environment limits their biomedical applications. This weakness could be conquered by alloying Co nanoparticles with Pt, resulting in a stable CoPt alloy. The magnetic property and MRI contrast ability of HCPA-NPs-PEG were then evaluated. Figure 2f shows that HCPA-NPs-PEG displays superparamagnetic behavior and has magnetic saturation value of  $50 \text{ emu g}^{-1}$  based on the Co content, which is comparable to that of previously reported solid CoPt nanoparticles.<sup>[14]</sup> As shown in Figure 4a,b, the images turned darker as the concentration of the HCPA-NPs-PEG increased. The transverse relaxivity ( $r_2$ ) of HCPA-NPs-PEG

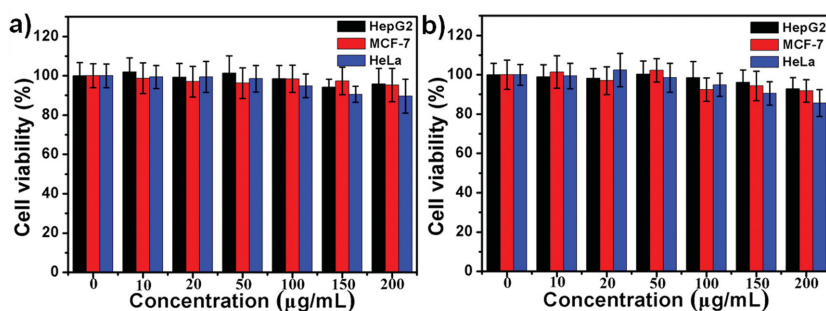


**Figure 3.** Relative cell viability of HepG2, MCF-7, and HeLa cells after being incubated with different concentrations of HCPA-NPs-PEG for a) 24 h and b) 48 h, then evaluated by CCK-8 assays.

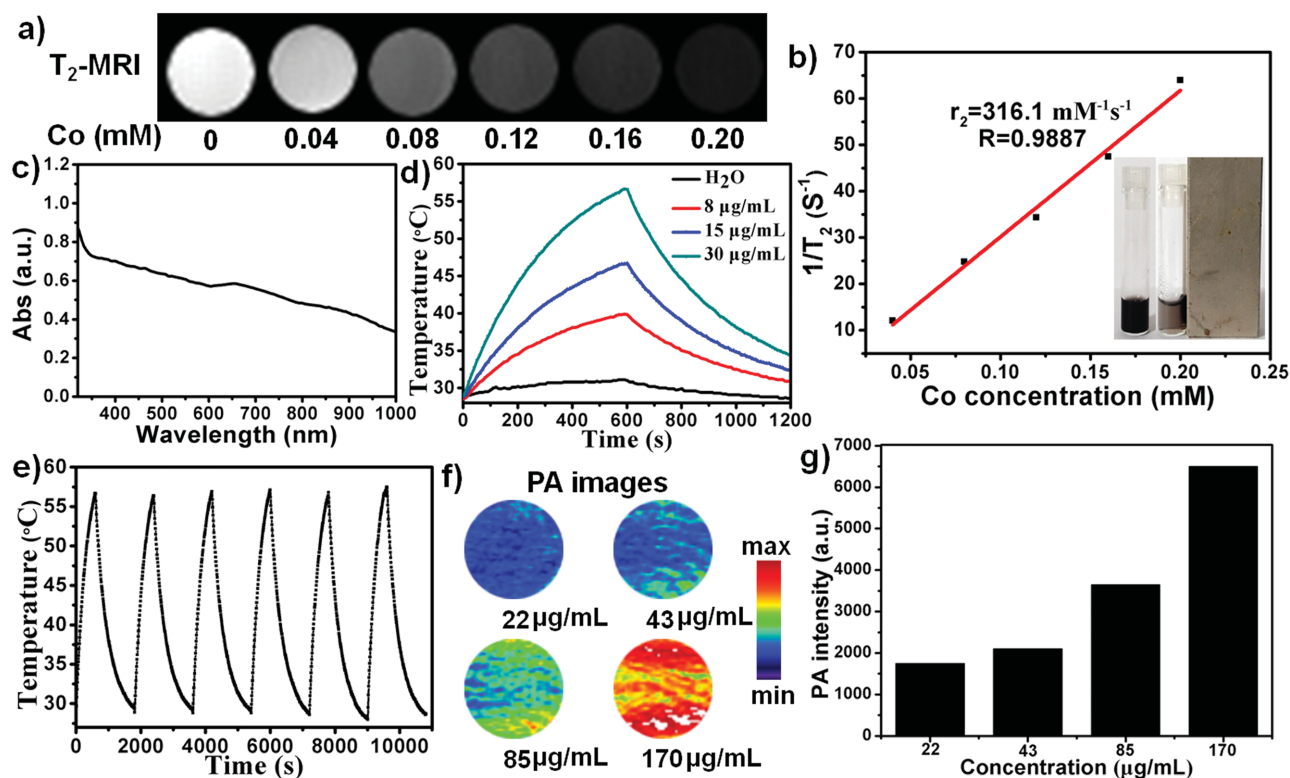


**Figure 4.** a)  $T_2$ -weighted MR images at 9.4 T of HCPA-NPs-PEG. b)  $T_2$  relaxation rates ( $r_2$ ) of HCPA-NPs-PEG solutions at different Co concentrations. The  $T_2$  relaxivity ( $r_2$ ) of HCPA-NPs-PEG was determined to be  $316.1 \times 10^{-3} \text{ m}^{-1} \text{ s}^{-1}$ . c) UV-vis-NIR absorption spectrum of  $60 \mu\text{g mL}^{-1}$  HCPA-NPs-PEG solution. d) Photothermal heating curves of the HCPA-NPs-PEG with different concentrations under 808 nm laser irradiation ( $1 \text{ W cm}^{-2}$ ). e) Photothermal heating curves of the HCPA-NPs-PEG over six cycles of NIR laser on/off. f) PA images and g) PA intensities of HCPA-NPs-PEG solutions with different concentrations.

was calculated to be  $316.1 \times 10^{-3} \text{ m}^{-1} \text{ s}^{-1}$ , which is higher than that of iron oxide nanoparticles with similar particle size.<sup>[15]</sup> These inspiring properties demonstrated that HCPA-NPs-PEG is an efficient and safe MRI contrast agent.

Nanomaterials that have inherent photo-based therapeutic capabilities are attracting much attention lately.<sup>[16]</sup> We next studied the optical characteristics of HCPA-NPs-PEG. As shown in Figure 4c, HCPA-NPs-PEG exhibited strong absorbance in the NIR region. The photothermal performance of HCPA-NPs-PEG was also investigated by measuring the temperature evolution of HCPA-NPs-PEG aqueous solutions under NIR laser irradiation (808 nm,  $1 \text{ W cm}^{-2}$ ). Figure 4d shows that the temperatures of HCPA-NPs-PEG solutions were elevated with the increase of the concentrations of HCPA-NPs-PEG and the laser irradiation time, while the pure water showed no obvious temperature change. Notably, the temperature of aqueous solution with  $30 \mu\text{g mL}^{-1}$  of HCPA-NPs-PEG reached  $57^\circ\text{C}$  after laser exposure for 10 min. Subsequently, the photothermal transduction efficiency of HCPA-NPs-PEG was calculated to be 33% (Figure S7, Supporting Information), which is higher than that of previously researched Au nanorods (Figure S8, Supporting Information, 21%).<sup>[17]</sup> Furthermore, the HCPA-NPs-PEG remained almost identical photothermal performance even after six cycles of laser on/off (Figure 4e), whereas Au nanorods showed poor thermal stability after laser irradiation.<sup>[18]</sup> As a burgeoning imaging tool, PAI provides not only good spatial resolution but also high imaging depth by using

contrast agents that have high NIR absorbance.<sup>[19]</sup> The PAI contrast ability of HCPA-NPs-PEG was then evaluated. As shown in Figure 4f,g, the brightness of PA images and the photoacoustic signals was enhanced with increased concentration of HCPA-NPs-PEG, demonstrating that HCPA-NPs-PEG can also be a good PAI contrast agent.

As a novel promising cancer therapy strategy, PTT can efficiently cause necrosis of cancer cells and ultimately eliminate tumors.<sup>[20]</sup> Moreover, recent studies have shown that PTT can induce immune responses to inhibit cancer metastasis.<sup>[21]</sup> The potential of HCPA-NPs-PEG to be a PTT agent was first examined by propidium iodide (PI) staining experiments. As shown in confocal laser scanning microscopy (CLSM) results (Figure 5a), more red fluorescence dots appeared as the laser irradiation time increased in the HCPA-NPs-PEG treated group, while only sporadic red fluorescence can be observed in the control group. We next determined cell viability to quantitatively evaluate the PTT effect of different concentrations of HCPA-NPs-PEG after laser irradiation for 10 min (808 nm,  $1 \text{ W cm}^{-2}$ ). The results showed that the laser irradiation only and HCPA-NPs-PEG only controls had low effects on the cell viability (Figure 5b); however, the cell viability sharply decreased when treated with HCPA-NPs-PEG and laser exposure. These good PTT performances of HCPA-NPs-PEG in vitro motivated us to further apply them for theranostic applications in vivo.

To realize the noninvasive and accurate imaging of tumor, the integration of MRI and PAI has become a promising

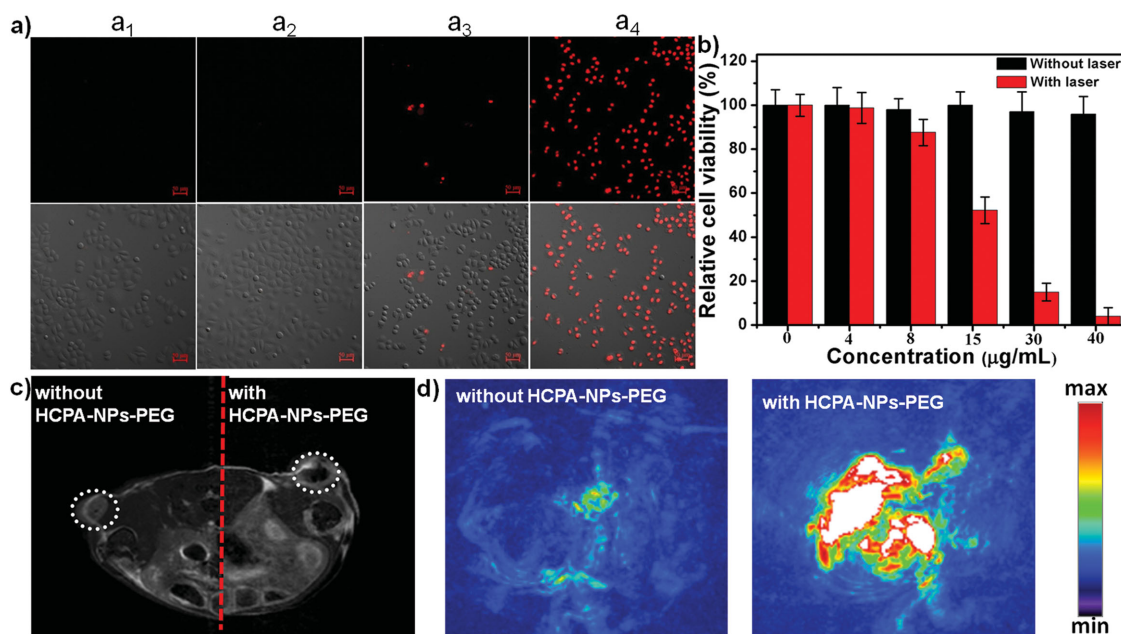


**Figure 5.** a) CLSM images of differently treated HepG2 cells stained with PI: top panels: PI fluorescence corresponding to dead cells, bottom panels: the overlay of PI fluorescence and the bright field image. a<sub>1</sub>) 8 min laser; a<sub>2</sub>) HCPA-NPs-PEG only; a<sub>3</sub>) HCPA-NPs-PEG plus 2 min laser; a<sub>4</sub>) HCPA-NPs-PEG plus 8 min laser. b) Cell viability of HepG2 cells exposed to different concentrations of HCPA-NPs-PEG with or without laser irradiation. c) Representative  $T_2$ -weighted MRI scans of mice: left tumor without the HCPA-NPs-PEG, right tumor with the HCPA-NPs-PEG (the tumor areas are marked by the white circle). d) PA images of tumor site without and with injection with HCPA-NPs-PEG.

strategy that offers high optical sensitivity and fine spatial resolution.<sup>[22]</sup> The HCPA-NPs-PEG was then used as a contrast agent for in vivo tumor MRI and PAI. Representative  $T_2$ -weighted MR images of a mouse bearing bilateral HepG2 tumors are shown in Figure 5c. The right tumor with HCPA-NPs-PEG injection displayed a much darker image than the left tumor without HCPA-NPs-PEG injection, indicating that the HCPA-NPs-PEG is a good MRI contrast agent to improve the imaging contrast in vivo. The in vivo PAI contrast ability of HCPA-NPs-PEG was evaluated by scanning tumors before and after the injection of HCPA-NPs-PEG (Figure 5d). Only the major blood vessels could be imaged without HCPA-NPs-PEG. By contrast, the tumor with HCPA-NPs-PEG injection showed a significantly brighter image around the tumor region. These observations suggest that HCPA-NPs-PEG is a good MRI/PAI dual-modality imaging contrast agent.

We finally utilized HCPA-NPs-PEG for in vivo tumor PTT. HepG2 tumor-bearing mice were randomly divided into three groups with four mice per group when the tumor size reached about 100 mm<sup>3</sup>. These mice were then treated as: I) control group, NIR laser only; II) HCPA-NPs-PEG only; III) HCPA-NPs-PEG plus NIR (laser: 808 nm; HCPA-NPs-PEG: 2 mg kg<sup>-1</sup>). The in vivo photothermal performance of HCPA-NPs-PEG was studied with an Infrared (IR) thermal camera (Figure 6a). After exposing the HCPA-NPs-PEG-treated mice to the NIR laser for 10 min, the tumor temperature was 20 °C above body temperature (Figure 6b). However, the temperature of tumor in mice without injection of HCPA-NPs-PEG showed little change after the same laser irradiation. Hematoxylin and eosin staining of tumor sections (Figure S9, Supporting Information) revealed that the tumor cells in NIR

laser only group and HCPA-NPs-PEG only group remained well-shaped cell morphology. In contrast, the tumor cells in the HCPA-NPs-PEG plus NIR group showed necrosis with cells deformation due to PTT. Therefore, the HCPA-NPs-PEG has no significant toxicity but still has a good photothermal performance in vivo. The body weights of all the mice were also recorded, showing no evident body weight loss during the treatment period (Figure 6c). Moreover, changes in tumor sizes were monitored by measuring the tumor size every other day with a caliper. The results in Figure 6d,e showed that tumors in HCPA-NPs-PEG plus NIR group were completely eliminated with no tumor re-growth after 16 d post treatment, while tumors in HCPA-NPs-PEG only group displayed rapid growth, similar to the tumors in the NIR laser only group. Particularly, the weights of mice treated with HCPA-NPs-PEG plus NIR have been monitored within 40 d. Neither death nor significant body weight drop was observed (Figure S10, Supporting Information). Furthermore, major organs of mice were collected 40 d after the treatment for histology analysis, showing no evident tissue damage in the mice treated with HCPA-NPs-PEG plus NIR compared to the control healthy mice without treatment (Figure S11, Supporting Information). These phenomena clearly suggest that the HCPA-NPs-PEG has good biocompatibility and can be used as a PTT agent for tumor therapy in vivo.

### 3. Conclusion

In summary, we developed a facile and green strategy for the synthesis of hollow CoPt alloy nanoparticles. This innovative synthetic strategy uses plant polyphenols that have robust

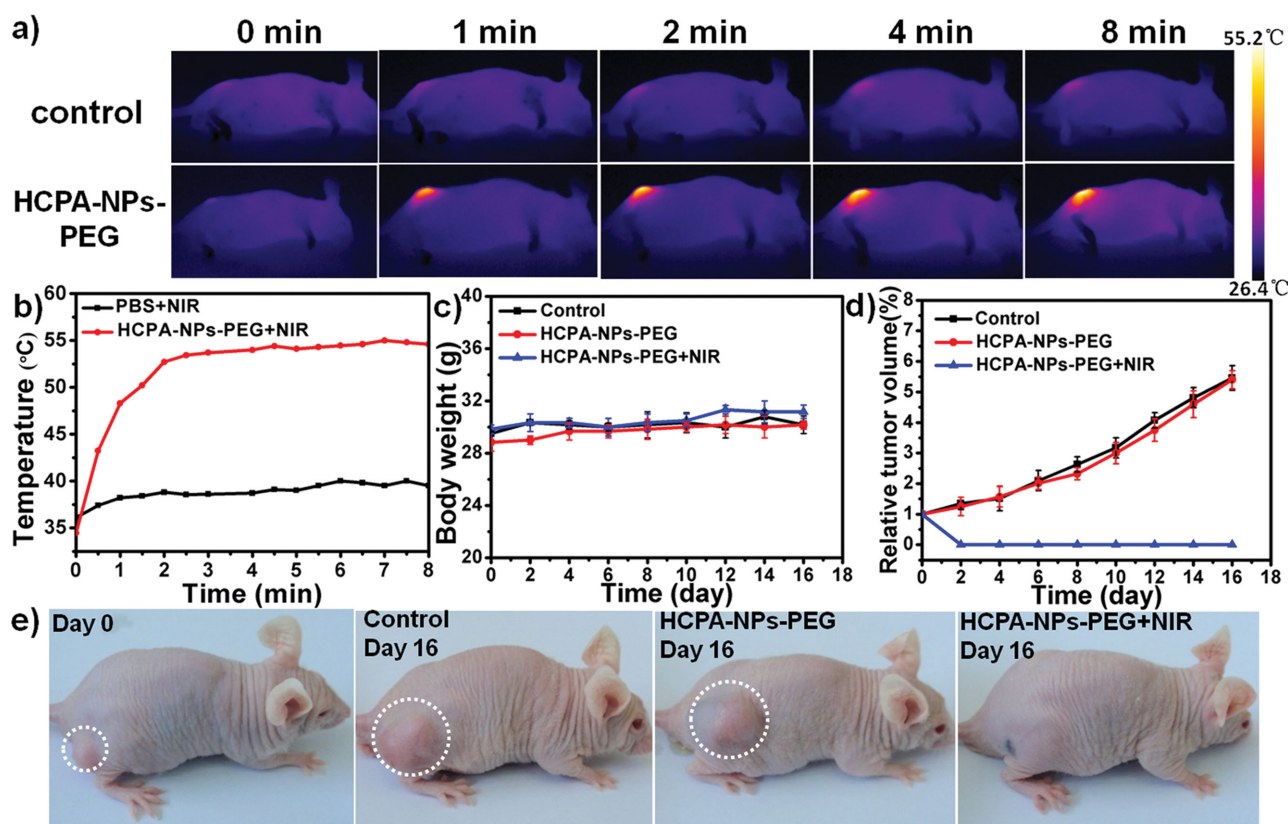


**Figure 6.** a) IR thermal images of tumor-bearing mice after injection with PBS or HCPA-NPs-PEG exposed to the 808 nm laser ( $0.75 \text{ W cm}^{-2}$ ) for different time. b) Tumor temperatures of mice monitored by the IR thermal camera as a function of the irradiation time. c) Body weights of mice in different groups. d) Tumor growth curves of different groups of tumor-bearing mice after treatment. e) Representative photos of different groups of mice before and after various treatments.

metal-chelating ability as assisted agents. It can be used to construct hollow alloy nanoparticles of different sizes by using polyphenols of different molecule sizes. The strategy can also enable the generation of other hollow alloy nanoparticles with different metal compositions. The synthesized HCPA-NPs have high  $T_2$  relaxivity, strong NIR absorbance, and good photothermal performances. We further demonstrated their ability to act as theranostic agents for MRI/PAI dual-modality imaging and PTT. Therefore, our work would extend potential applications of hollow alloy nanomaterials for theranostic applications. Moreover, this strategy is simple, inexpensive, size tunable and versatile. It will draw tremendous attention in a variety of fields including catalysis, magnetic-storage, electronics, and biomedical applications.

#### 4. Experimental Section

**Chemicals:** Cobalt (II) chloride hexahydrate ( $\text{CoCl}_2 \cdot 6\text{H}_2\text{O}$ ) and TA were purchased from Sinopharm Chemical Reagent Co. Ltd. (China). Potassium tetrachloroplatinate (II) ( $\text{K}_2\text{PtCl}_4$ ), EGCG, and EA were purchased from Sigma-Aldrich. **The dopamine modified PEG (DA-PEG, MW 2000) was purchased from Xi'an Ruixi Biological Technology Co. Ltd. (China).** All the other chemicals were of analytical grade and were used as received. Ultrapure water obtained from a Millipore water purification system ( $18.2 \text{ M}\Omega$  resistivity) was used in all runs.

**Apparatus:** Ultraviolet-visible (UV-vis)-NIR absorption spectra were recorded using a SH-1000 Lab microplate reader (Corona Electric, Hitachinaka, Japan) at room temperature. A semiconductor laser unit (KS3-11312-110, BWT, Beijing Kaipulin Co. Ltd., China) was used for photothermal irradiation. The fluorescence images of cells were taken on a confocal fluorescence microscope (Nikon C2). The thermal images were obtained using FLIR A35 thermal camera.

**Preparation of HCPA-NPs-PEG:** All used solutions of polyphenols were freshly prepared for immediate use. HCPA-NPs was synthesized through the co-reduction of  $2 \times 10^{-3} \text{ M}$   $\text{CoCl}_2 \cdot 6\text{H}_2\text{O}$  and  $2 \times 10^{-3} \text{ M}$   $\text{K}_2\text{PtCl}_4$  in aqueous solutions containing  $2 \text{ mg mL}^{-1}$  polyphenols by  $\text{NaBH}_4$ . The reaction mixture was sonicated for 30 min before centrifuging and washing with water for three times. The obtained HCPA-NPs were then mixed with  $2 \text{ mg mL}^{-1}$  DA-PEG and stirred overnight to get HCPA-NPs-PEG. Hollow NiPt alloy nanoparticles were synthesized by using TA as assisted agents according to the above method, except using  $\text{NiCl}_2$  to replace  $\text{CoCl}_2 \cdot 6\text{H}_2\text{O}$ . The mass concentration of HCPA-NPs-PEG was measured using the gravimetric method, and the molar concentration of cobalt was measured by inductively coupled plasma mass spectrometry (ICP-MS).

**Preparation of Gold Nanorods (Au NRs):** According to the previous method,<sup>[17b]</sup> the seed solution was first synthesized by adding  $\text{HAuCl}_4$  (0.01 M, 0.25 mL) to the solution of cetyltrimethylammonium bromide (CTAB, 0.1 M, 10 mL). A freshly prepared, ice-cold  $\text{NaBH}_4$  solution (0.01 M, 0.6 mL) was then added into the

mixture solution under stirring for 2 h. To grow Au NRs, HAuCl<sub>4</sub> (0.01 M, 4.0 mL) were first incubated with AgNO<sub>3</sub> (0.01 M, 0.8 mL), CTAB solution (0.1 M, 80 mL), and HCl (1.0 M, 1.6 mL), followed by the addition of ascorbic acid (0.1 M, 0.64 mL). Finally, the seed solution (192 μL) was injected into the growth solution, and the solution was gently mixed for 30 s and left undisturbed at 27–30 °C for 6 h to obtain the desired Au NRs.

**Cellular Experiments:** For cytotoxicity assay, HepG2, MCF-7, and HeLa cells were cultured in RPMI-1640 medium (Gibco) plus 10% fetal bovine serum (Gibco) at 37 °C in a humidified atmosphere with 5% CO<sub>2</sub>. In a typical experiment of the cytotoxicity assay, HepG2 cells were seeded in 96-well plates and incubated overnight at 37 °C in a humidified 5% CO<sub>2</sub> atmosphere. The cells were then incubated with 100 μL of various concentrations of HCPA-NPs-PEG for 24 h at 37 °C in the dark. Cell viabilities were determined by CCK-8 according to the manufacture's protocol. For PI staining experiments, HepG2 cells were incubated with various concentrations of HCPA-NPs-PEG for 4 h, followed by exposing to 808 nm laser irradiation. Then the cells were imaged by confocal laser scanning microscopy after PI staining.

**Measurement of the Photothermal Performance:** The photothermal performance was investigated by recording the temperature changes of the solution under continuous laser irradiation. In a typical experiment, 1 mL aqueous dispersions of HCPA-NPs-PEG with different concentrations were irradiated by 808 nm laser for 10 min (1 W cm<sup>-2</sup>). The temperature changes were monitored by a digital thermometer during the irradiation period. The photothermal conversion efficiency ( $\eta$ ) was calculated according to Equation (1) in previous methods<sup>[16d]</sup>

$$\eta = \frac{hA\Delta T_{\max} - Q_s}{I(1 - 10^{-A_{808}})} \quad (1)$$

Where  $\Delta T_{\max}$  is the temperature change at the maximum steady-state temperature,  $Q_s$  is the heat dissipation from the light absorbance of the solvent,  $I$  is the laser power (1 W cm<sup>-2</sup>),  $A_{808}$  is the absorbance of the determined HCPA-NPs-PEG solution at 808 nm.  $hA$  is determined by the following Equation (2)

$$\tau_s = \frac{m_D C_D}{hA} \quad (2)$$

Where  $\tau_s$  is sample system time constant that can be obtained from the cooling period versus  $-\ln(\Delta T/\Delta T_{\max})$ ,  $m_D$  and  $C_D$  are the mass (1 g) and heat capacity (4.2 J g<sup>-1</sup>) of the used solvent. Using the above two equations, the photothermal conversion efficiency ( $\eta$ ) of nanoparticles can be calculated.

**Measurement of MRI Relaxation Properties:** To measure the  $T_2$  relaxation properties, HCPA-NPs-PEG with different cobalt concentrations were prepared in 1% agarose solution and measured using a Bruker 9.4T small animal MRI scanner (94/20 USR, Bruker, Germany). The relaxation rate  $r_2$  was determined from the slope of  $1/T_2$  values as the function of cobalt concentrations.  $T_2$ -weighted MR images were acquired using a fast spin echo sequence with the following parameters: TR/TE = 1000/8.5 ms, 256 × 256 matrices, repetition time 1.

**In Vivo MRI and PAI:** All the animal experiments were carried out under protocols approved by Xiamen University Laboratory Animal Center. BALB/c nude mice (weight ≈30 g) were obtained from Shanghai SLAC laboratory Animal Co., Ltd. Tumor-bearing

mice were prepared by subcutaneously injecting a suspension of 2 × 100 HepG2 cells in phosphate buffered saline (PBS) (100 μL) into the back of the hind leg. All mice were anesthetized with 1%–2% isoflurane mixed with pure oxygen via a nose cone before imaging. For in vivo MRI, axial and coronal 2D fast spin echo sequence images were first acquired to ensure the imaging position of the tumors. The following parameters were adopted for  $T_2$ -weighted multislice spinecho images: TR/TE = 1000/8.5 ms, matrix = 256 × 256, 9 contiguous slices. In vivo PAI was performed with an Endra Life Sciences Nexus128 instrument, which produced 3D photoacoustic images by a hemispherical ultrasonic detector with 128 identical ultrasonic transducers spirally installed on the surface. PA images were scanned with and without the injection of HCPA-NPs-PEG.

**In Vivo PTT:** All mice were divided into three groups with four mice per group when the tumor size reached about 100 mm<sup>3</sup>. The mice were intratumorally injected with 50 μL of PBS and HCPA-NPs-PEG, respectively (HCPA-NPs-PEG 2 mg kg<sup>-1</sup>). After injections, tumors were irradiated with or without NIR laser (808 nm, 0.75 W cm<sup>-2</sup>) for 10 min. Infrared thermal imaging system was performed for studying the photothermal effect of HCPA-NPs-PEG in vivo. The tumor sizes were measured by a digital caliper every other day. The tumor volumes were calculated through the equation: volume =  $ab^2/2$ , where  $a$  and  $b$  are the maximum diameter and the minimum diameter of tumor, respectively. Relative tumor volumes were calculated as  $V/V_0$ , where  $V_0$  is the tumor volume when the treatment was initiated. The body weights of mice were also measured every other day.

**Histology Analysis:** Animals with tumors were sacrificed and collected after PTT for histological examination using hematoxylin and eosin (H&E) staining method.

## Supporting Information

Supporting Information is available from the Wiley Online Library or from the author.

## Acknowledgements

This work was supported by the National Basic Research Program of China (Grant Nos. 2010CB732403 and 2014CB744503), the National Natural Science Foundation of China (Grant Nos. 21125524, 21475026, 81422023, and 51273165), the Program for New Century Excellent Talents in University (NCET-13-0502), and the Fundamental Research Funds for the Central Universities (2013121039).

- [1] a) S. Goel, F. Chen, W. Cai, *Small* **2014**, *10*, 631; b) A. Schroeder, D. A. Heller, M. M. Winslow, J. E. Dahlman, G. W. Pratt, R. Langer, T. Jacks, D. G. Anderson, *Nat. Rev. Cancer* **2012**, *12*, 39; c) J. Li, C. Zheng, S. Cansiz, C. Wu, J. Xu, C. Cui, Y. Liu, W. Hou, Y. Wang, L. Zhang, I. T. Teng, H. H. Yang, W. Tan, *J. Am. Chem. Soc.* **2015**, *137*, 1412; d) R. Bardhan, S. Lal, A. Joshi, N. J. Halas, *Acc. Chem. Res.* **2011**, *44*, 936.

- [2] a) Y. Liu, J. R. Ashton, E. J. Moding, H. Yuan, J. K. Register, A. M. Fales, J. Choi, M. J. Whitley, X. Zhao, Y. Qi, Y. Ma, G. Vaidyanathan, M. R. Zalutsky, D. G. Kirsch, C. T. Badea, T. Vo-Dinh, *Theranostics* **2015**, *5*, 946; b) H. M. Meng, L. M. Lu, X. H. Zhao, Z. Chen, Z. L. Zhao, C. Yang, X. B. Zhang, W. H. Tan, *Anal. Chem.* **2015**, *87*, 4448; c) M. Satpathy, L. Wang, R. Zielinski, W. Qian, M. Lipowska, J. Capala, G. Y. Lee, H. Xu, A. Wang, H. Mao, L. Yang, *Small* **2014**, *10*, 544; d) L. S. Lin, Z. X. Cong, J. Li, K. M. Ke, S. S. Guo, H. H. Yang, G. N. Chen, *J. Mater. Chem.* **2014**, *2*, 1031.
- [3] a) M. A. Mahmoud, R. Narayanan, M. A. El-Sayed, *Acc. Chem. Res.* **2013**, *46*, 1795; b) X. Xia, Y. Wang, A. Ruditskiy, Y. Xia, *Adv. Mater.* **2013**, *25*, 6313.
- [4] a) D. Ho, X. Sun, S. Sun, *Acc. Chem. Res.* **2011**, *44*, 875; b) K. An, T. Hyeon, *Nano Today* **2009**, *4*, 359.
- [5] a) M. Grzelczak, J. Pérez-Juste, P. Mulvaney, L. M. Liz-Marzán, *Chem. Soc. Rev.* **2008**, *37*, 1783; b) S. J. Soenen, P. Rivera-Gil, J. M. Montenegro, W. J. Parak, S. C. De Smedt, K. Braeckmans, *Nano Today* **2011**, *6*, 446.
- [6] a) W. S. Wang, M. Dahl, Y. D. Yin, *Chem. Mater.* **2013**, *25*, 1179; b) G. Xiao, Y. Zeng, Y. Jiang, J. Ling, W. Zheng, B. Liu, X. Chen, G. Zou, B. Zou, *Small* **2013**, *9*, 793.
- [7] T. S. Sileika, D. G. Barrett, R. Zhang, K. H. A. Lau, P. B. Messersmith, *Angew. Chem.* **2013**, *125*, 10966; *Angew. Chem. Int. Ed.* **2013**, *52*, 10766.
- [8] a) S. Iravani, *Green Chem.* **2011**, *13*, 2638; b) J. L. Guo, Y. Ping, H. Ejima, K. Alt, M. Meissner, J. J. Richardson, Y. Yan, K. Peter, D. von Elverfeldt, C. E. Hagemeyer, F. Caruso, *Angew. Chem.* **2014**, *126*, 5652; *Angew. Chem. Int. Ed.* **2014**, *53*, 5546.
- [9] J. Gu, Y. W. Zhang, F. F. Tao, *Chem. Soc. Rev.* **2012**, *41*, 8050.
- [10] a) T. L. Le, L. D. Tung, J. Long, D. G. Fernig, N. T. K. Thanh, *J. Mater. Chem.* **2009**, *19*, 6023; b) C. Y. Song, Y. Wang, N. L. Rosi, *Angew. Chem.* **2013**, *125*, 4085; *Angew. Chem. Int. Ed.* **2013**, *52*, 3993; c) Y. Vasquez, A. K. Sra, R. E. Schaak, *J. Am. Chem. Soc.* **2005**, *127*, 12504.
- [11] C. Brandenberger, C. Muhlfeld, Z. Ali, A. G. Lenz, O. Schmid, W. J. Parak, P. Gehr, B. Rothen-Rutishauser, *Small* **2010**, *6*, 1669.
- [12] a) H. T. Jiang, F. Liu, H. L. Yang, Y. Li, *Biol. Trace Elem. Res.* **2012**, *146*, 23; b) Y. Lu, Y. Zhao, L. Yu, L. Dong, C. Shi, M. J. Hu, Y. J. Xu, L. P. Wen, S. H. Yu, *Adv. Mater.* **2010**, *22*, 1407; c) X. T. Meng, H. C. Seton, L. T. Lu, I. A. Prior, N. T. K. Thanh, B. Song, *Nanoscale* **2011**, *3*, 977.
- [13] a) L. S. Bouchard, M. S. Anwar, G. L. Liu, B. Hann, Z. H. Xie, J. W. Gray, X. D. Wang, A. Pines, F. F. Chen, *Proc. Natl. Acad. Sci. USA* **2009**, *106*, 4085; b) J. Li, C. Y. Hong, S. X. Wu, H. Liang, L. P. Wang, G. M. Huang, X. Chen, H. H. Yang, D. H. Shangguan, W. H. Tan, *J. Am. Chem. Soc.* **2015**, *137*, 11210.
- [14] S. N. Yin, Z. W. Li, L. Cheng, C. Wang, Y. M. Liu, Q. Chen, H. Gong, L. Guo, Y. G. Li, Z. Liu, *Nanoscale* **2013**, *5*, 12464.
- [15] a) D. A. Herman, P. Ferguson, S. Cheong, I. F. Hermans, B. J. Ruck, K. M. Allan, S. Prabakar, J. L. Spencer, C. D. Lendrum, R. D. Tilley, *Chem. Commun.* **2011**, *47*, 9221; b) S. Cheong, P. Ferguson, K. W. Feindel, I. F. Hermans, P. T. Callaghan, C. Meyer, A. Slocombe, C. H. Su, F. Y. Cheng, C. S. Yeh, B. Ingham, M. F. Toney, R. D. Tilley, *Angew. Chem.* **2011**, *123*, 4292; *Angew. Chem. Int. Ed.* **2011**, *50*, 4206.
- [16] a) Q. Shao, B. G. Xing, *Chem. Soc. Rev.* **2010**, *39*, 2835; b) X. H. Huang, I. H. El-Sayed, W. Qian, M. A. El-Sayed, *J. Am. Chem. Soc.* **2006**, *128*, 2115; c) S. G. Hou, L. Liang, S. H. Deng, J. F. Chen, Q. Huang, Y. Cheng, C. H. Fan, *Sci. China: Chem.* **2014**, *57*, 100; d) Z. B. Zha, X. L. Yue, Q. S. Ren, Z. F. Dai, *Adv. Mater.* **2013**, *25*, 777.
- [17] a) C. M. Hessel, V. P. Pattani, M. Rasch, M. G. Panthani, B. Koo, J. W. Tunnell, B. A. Korgel, *Nano Lett.* **2011**, *11*, 2560; b) Y. Liu, K. Ai, J. Liu, M. Deng, Y. He, L. Lu, *Adv. Mater.* **2013**, *25*, 1353.
- [18] a) L. M. Nie, S. J. Wang, X. Y. Wang, P. F. Rong, A. Bhirde, Y. Ma, G. Liu, P. Huang, G. M. Lu, X. Y. Chen, *Small* **2014**, *10*, 1585; b) H. Moon, D. Kumar, H. Kim, C. Sim, J. H. Chang, J. M. Kim, H. Kim, D. K. Lim, *ACS Nano* **2015**, *9*, 2711.
- [19] a) L. H. V. Wang, S. Hu, *Science* **2012**, *335*, 1458; b) G. Ku, M. Zhou, S. L. Song, Q. Huang, J. Hazle, C. Li, *ACS Nano* **2012**, *6*, 7489; c) A. De La Zerda, C. Zavaleta, S. Keren, S. Vaithilingam, S. Bodapati, Z. Liu, J. Levi, B. R. Smith, T. J. Ma, O. Oralkan, Z. Cheng, X. Y. Chen, H. J. Dai, B. T. Khuri-Yakub, S. S. Gambhir, *Nat. Nanotechnol.* **2008**, *3*, 557.
- [20] a) Y. W. Wang, Y. Y. Fu, Q. L. Peng, S. S. Guo, G. Liu, J. Li, H. H. Yang, G. N. Chen, *J. Mater. Chem.* **2013**, *1*, 5762; b) J. Li, F. Jiang, B. Yang, X. R. Song, Y. Liu, H. H. Yang, D. R. Cao, W. R. Shi, G. N. Chen, *Sci. Rep.* **2013**, *3*, 1998; c) J. F. Lovell, C. S. Jin, E. Huynh, H. L. Jin, C. Kim, J. L. Rubinstein, W. C. W. Chan, W. G. Cao, L. V. Wang, G. Zheng, *Nat. Mater.* **2011**, *10*, 324.
- [21] C. Wang, L. G. Xu, C. Liang, J. Xiang, R. Peng, Z. Liu, *Adv. Mater.* **2014**, *26*, 8154.
- [22] a) L. S. Lin, Z. X. Cong, J. B. Cao, K. M. Ke, Q. L. Peng, J. H. Gao, H. H. Yang, G. Liu, X. Y. Chen, *ACS Nano* **2014**, *8*, 3876; b) J. Rieffel, U. Chitgupi, J. F. Lovell, *Small* **2015**, *11*, 4445; c) X. R. Song, X. Y. Wang, S. X. Yu, J. B. Cao, S. H. Li, J. Li, G. Liu, H. H. Yang, X. Y. Chen, *Adv. Mater.* **2015**, *27*, 3285.

Received: October 27, 2015  
 Revised: December 16, 2015  
 Published online: